Ion-kinetic simulations of D-^{3}He gas-filled inertial confinement fusion target implosions with moderate to large Knudsen number

O. Larroche [ID], H. G. Rinderknecht [ID], M. J. Rosenberg, N. M. Hoffman [ID], S. Atzeni [ID], R. D. Petrasso [ID], P. A. Amendt, and F. H. Séguin

View Online   Export Citation   CrossMark

ARTICLES YOU MAY BE INTERESTED IN

Ion-kinetic simulations of D-³He gas-filled inertial confinement fusion target implosions with moderate to large Knudsen number

O. Larroche,[1] H. G. Rinderknecht,[2] M. J. Rosenberg,[3] N. M. Hoffman,[4] S. Atzeni,[5] R. D. Petrasso,[6] P. A. Amendt,[2] and F. H. Séguin[6]

[1]*CEA DIF, 91297 Arpajon Cedex, France*
[2]*Lawrence Livermore National Laboratory, Livermore, California 94550, USA*
[3]*Laboratory for Laser Energetics, University of Rochester, Rochester, New York 14623, USA*
[4]*Los Alamos National Laboratory, Los Alamos, New Mexico 87545, USA*
[5]*Dipartimento SBAI, Università di Roma "La Sapienza" and CNISM, Via A. Scarpa 14-16, I-00161 Roma, Italy*
[6]*Plasma Science and Fusion Center, Massachusetts Institute of Technology, Cambridge, Massachusetts 02139, USA*

Experiments designed to investigate the transition to non-collisional behavior in D³He-gas inertial confinement fusion target implosions display increasingly large discrepancies with respect to simulations by standard hydrodynamics codes as the expected ion mean-free-paths λ_c increase with respect to the target radius R (i.e., when the Knudsen number $N_K = \lambda_c/R$ grows). To take properly into account large N_K's, multi-ion-species Vlasov-Fokker-Planck computations of the inner gas in the capsules have been performed, for two different values of N_K, one moderate and one large. The results, including nuclear yield, reactivity-weighted ion temperatures, nuclear emissivities, and surface brightness, have been compared with the experimental data and with the results of hydrodynamical simulations, some of which include an *ad hoc* modeling of kinetic effects. The experimental results are quite accurately rendered by the kinetic calculations in the smaller-N_K case, much better than by the hydrodynamical calculations. The kinetic effects at play in this case are thus correctly understood. However, in the higher-N_K case, the agreement is much worse. The remaining discrepancies are shown to arise from kinetic phenomena (e.g., inter-species diffusion) occurring at the gas-pusher interface, which should be investigated in the future work. © 2016 AIP Publishing LLC. [http://dx.doi.org/10.1063/1.4939025]

I. INTRODUCTION

After the completion of the National Ignition Campaign[1] on the National Ignition Facility (NIF), emphasis was put on various physical mechanisms at play in the physics of Inertial Confinement Fusion[2–4] (ICF) which might explain why full ignition of thermonuclear combustion could not be reached in these experiments. Among these, some concern was drawn to the fact that the collisional mean-free paths of the ions in the ICF target material were possibly not small enough for the numerical modeling of them by standard hydrodynamics to be fully valid in certain phases of the implosion (particularly the first shock convergence phase) as well as to the possible significance of multiple-ion-species dynamics not modeled by standard hydrodynamics. The ignition target design optimization[5,6] conducted on the basis of these calculations was thus invalidated. Specific experiments were then designed and fielded both on the NIF[7] and OMEGA[8–11] laser facilities to investigate a regime of purposely lower collisionality, where such kinetic and multi-species effects were indeed expected to be exaggerated, and to examine if and how they could be appropriately rendered by available numerical models. The OMEGA experiments, in which the least collisional implosions were performed, are briefly reviewed in Sec. II, together with state-of-the-art hydrodynamical modeling of them.

The general conclusion of this experimental program is that as the Knudsen number (the ratio N_K of the relevant collisional mean-free path λ_c to a typical scale length R of the system) is increased, a strongly growing discrepancy is observed between the experimentally measured observables and their values, as found in the hydrodynamical modeling. This discrepancy can be reduced to some extent using a heuristic description of kinetic effects (the so-called "Reduced-Ion-Kinetic" (RIK) model[12]), provided the free parameters in this model are appropriately adjusted. These results confirm and extend the trend observed in the "Polar Direct Drive" implosions on NIF.[7]

A need for more fundamental, fully kinetic modeling of these systems thus arises, in order to get a firm, basic reference description from which the heuristic modeling used in hydrodynamical codes might tentatively be justified and tuned up. Such a modeling, resting on a Vlasov-Fokker-Planck (VFP) numerical model of ion kinetics,[13,14] is presented in this paper. The kinetic simulation process is described in Sec. III, and results in the case of D³He gas target implosions from Refs. 8 and 9, for two different values of the Knudsen number, are presented in Sec. IV. Section V discusses these results, particularly the fact that the agreement with experimental data, while quite satisfactory in the lower-N_K case, is much worse for larger N_K. Section VI summarizes the results and suggests a path to

an improved rendering of kinetic effects in the larger-N_K targets.

II. A SUMMARY OF EXPERIMENTAL DATA AND HYDRODYNAMICAL SIMULATION RESULTS

A. Experiments

SiO$_2$ shells filled with equimolar D^{3}He gas at an initial density ranging from 0.14 to 3.1 mg/cm^3 (and up to 3.3 mg/cm^3 in some cases[11]) were imploded by direct drive of 14.6 kJ, 0.6 ns flat-top laser pulses. Such laser powers typically generate a strong shock propagating into the gas, so that the hydrodynamical stability is not a concern in these experiments. In addition, the implosion can be assumed to maintain spherical symmetry;[10] hence, all quantities discussed in this paper will be expressed as functions of the radial distance r from the center of the target only. Nuclear diagnostics use the high-energy neutrons and protons from the reactions

$$D + D \rightarrow T + p \,(3.02\,\text{MeV}), \tag{1}$$

$$D + D \rightarrow {}^3He + n \,(2.45\,\text{MeV}), \tag{2}$$

$$D + {}^3He \rightarrow {}^4He + p \,(14.7\,\text{MeV}). \tag{3}$$
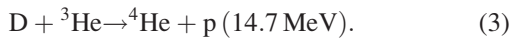
The basic quantity characterizing these reactions is the reactivity $R_{ij}(r,t)$, which is the number of reactions between ions of species i and j per unit volume and unit time, at radial position r and time t. The detailed function $R_{ij}(r,t)$ cannot be directly measured in experiments, but some information about it can be extracted from the actual diagnostics. Penumbral proton images lead to reconstructed time-integrated burn profiles[15] of the implosion, enabling the extraction of the time-integrated reactivity

$$E_{ij}(r) = \int_{-\infty}^{\infty} R_{ij}(r,t)dt \tag{4}$$

(total number of reactions per unit volume recorded over time at a given radius), called the "emissivity" in Ref. 9, and the time-integrated projection of the reaction rate along the line of sight

$$B_{ij}(r) = \int_{-\infty}^{\infty} E_{ij}(\sqrt{r^2+s^2})ds \tag{5}$$

(total number of reactions recorded over time per unit surface across the line of sight as a function of radius), called the "surface brightness" in Ref. 9. The overall reaction yields are the time- and space-integrals of the reactivity

$$Y_{ij} = \int_0^{\infty} E_{ij}(r)4\pi r^2 dr, \tag{6}$$

while the median burn radius R_{50} is defined for each reaction as the radius of the sphere enclosing 50% of the yield, thus

$$\int_0^{R_{50}} E_{ij}(r)4\pi r^2 dr = 0.50 \times Y_{ij}. \tag{7}$$

TABLE I. Summary of experimental data and simulation results in D^{3}He implosions for a high initial gas density $\rho = 3.1$ mg/cm^3 (experiments, DUED, and RIK simulations) or $\rho = 3.3$ mg/cm^3 (FPION simulations). The RIK values are obtained using the "4-shot model" described in Sec. III D of Ref. 12. The DUED values are obtained using a viscosity flux limiter of 0.25 (see Ref. 9) which produces the best agreement with the experimental burn profile shapes. The DUED burn-averaged temperatures are calculated taking into account the fluid motion of the gas.

	Exp.	DUED	RIK	FPION
DD-n yield (10^{10})	2.8	7.4	4.0	2.5
D^{3}He yield (10^{10})	3.4	5.8	2.6	2.4
T_{DD-n} (keV)	11.7	10.3	10.5	8.8
T_{D^3He} (keV)	14.1	12.8	11.6	12.8
$R_{50\,DD-p}$ (μm)	114	62	58	95
$R_{50\,D^3He}$ (μm)	74	47	34	72

Finally, reaction-weighted temperatures of the fuel ions T_{DD-n} and T_{D^3He} are deduced from the width of the corresponding collected product-particle spectra.[16,17] The experimentally measured values of these quantities for targets with two different values of the initial gas density are gathered in Tables I and II.

B. Hydrodynamical simulations used in this work

Hydrodynamical simulations performed with the code DUED[18,19] without RIK corrections are accounted for in Refs. 8 and 9. A set of numerical results discussed in this paper is listed in Tables I and II, under the heading "DUED." Some RIK-corrected[12] simulations tuned against a set of experimental data (namely, DD-n and D^{3}He yields, DD bang time, DD-averaged ion temperature, and laser absorption fraction) from several capsules have also been performed. The data available from Appendix B of Ref. 9 are also displayed in the tables, under the heading "RIK." It can be seen that they fail to render the burn radii, in both the low- and high-density cases.

In addition to the integrated quantities displayed in the tables, Ref. 9 also presents some detailed profiles of the emissivity and surface brightness. They will be discussed in relation with their counterparts from FPION in Secs. IV and V.

C. Simulation analysis with respect to collisionality

Among the various targets imploded with the same general parameters as mentioned in Sec. II A, two cases were

TABLE II. Summary of experimental data and simulation results in D^{3}He implosions for a low initial gas density $\rho = 0.4$ mg/cm^3. The RIK values are obtained using the "4-shot model" described in Sec. III D of Ref. 12. The DUED values are obtained using a viscosity flux limiter of 0.25 (see Ref. 9) which produces the best agreement with the experimental burn profile shapes.

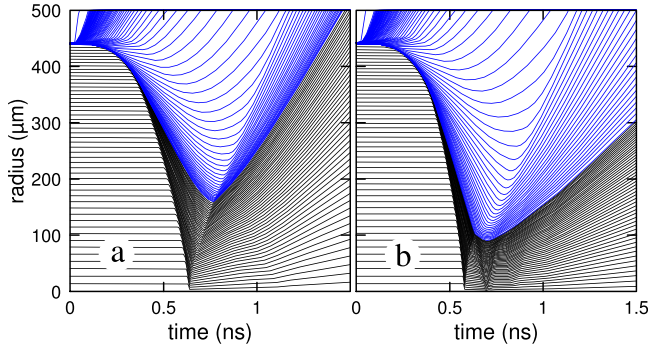|	Exp.	DUED	RIK	FPION
DD-n yield (10^{10})	0.55	8.2	0.13	4.4
D^{3}He yield (10^{10})	2.3	41	0.82	15.7
T_{DD-n} (keV)	20	29	26.1	20.5
T_{D^3He} (keV)	23	31	27.6	22.2
$R_{50\,DD-p}$ (μm)	77	49	42	68
$R_{50\,D^3He}$ (μm)	50	48	30	71

FIG. 1. Lagrangian diagram of the hydrodynamical simulation of the implosion in the high-density (a) and low-density (b) cases.

selected for kinetic simulations, namely, one closer to hydro-dynamical behaviour, with a higher initial density in the fuel (3.3 mg/cm³), and one where strong kinetic effects were expected, with a lower initial density (0.4 mg/cm³). A post-processing analysis of data from the hydrodynamical simulations of these two targets is presented and discussed in the following.

Fig. 1 displays a Lagrangian diagram of the implosion in both cases. In the low-density case, the main imploding shock velocity is seen to be much higher than in the high-density case, convergence occurs earlier, and the fuel radius at stagnation is much smaller.

As a result, the ion temperature reached in the fuel around stagnation is much higher in the low-density case, as displayed in Fig. 2. In both cases, a very steep drop in ion temperature occurs at the fuel/pusher interface. Such a large temperature gradient is not expected to be physically realistic, as discussed further below.

The electron temperature remains much lower and, after shock convergence, is fairly homogeneous in the whole target in both cases, due to the high thermal conductivity of electrons (see Fig. 3). As a result, the fuel/pusher interface is barely visible on these diagrams.

The Knudsen number can be estimated from these simulations by comparing the local value of the mean-free path for Coulomb collisions λ_c with the relevant dimensions in

the system. Fig. 4 displays space-time maps of λ_c for a thermal D ion, i.e., an ion moving with respect to the ambient fluid at velocity $v_{th} = \sqrt{k_B T_i / m_D}$, where T_i is the local value of the ion temperature and m_D is the mass of a deuteron. The calculation is done taking into account all species present at each point, in the fuel as well as in the pusher material, using the following expressions:

$$\lambda_c = \frac{v_{th}}{\sum_i \nu_{Di} + \nu_{De}},$$

where the sum is overall ion species present at a given point and

$$\nu_{Di} \sim 2.1 \times 10^{-12} \frac{n_i A_i^{1/2} Z_i^2 \operatorname{Log} \Lambda_{Di}}{T_i^{3/2}}$$

is the collision frequency (in s⁻¹) between a thermal D ion and the population of ions of species i with mass number A_i and charge number Z_i, and

$$\nu_{De} \sim 5 \times 10^{-14} \frac{n_e \operatorname{Log} \Lambda_{De}}{T_e^{3/2}}$$

FIG. 3. Space-time plot of the electron temperature in the hydrodynamical simulation of the implosion in the high-density (left) and low-density (right) cases.
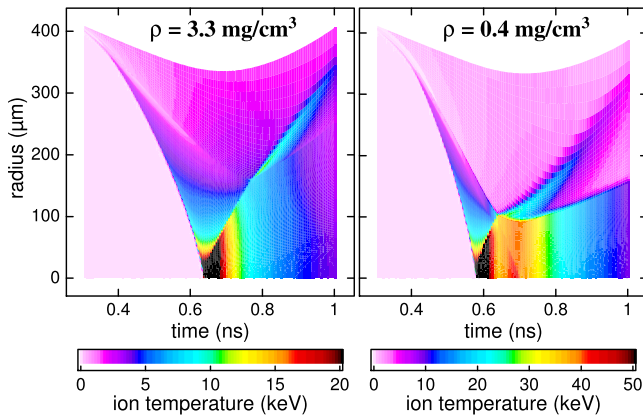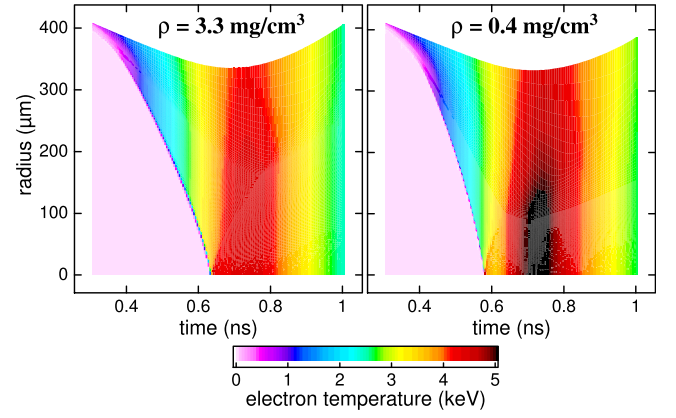

FIG. 2. Space-time plot of the ion temperature in the hydrodynamical simulation of the implosion in the high-density (left) and low-density (right) cases. Note that the temperature scale was clipped in both cases (to ≤20 keV in the high-density case and ≤50 keV in the low-density case) to display more clearly the range of temperatures reached in most of the diagram.
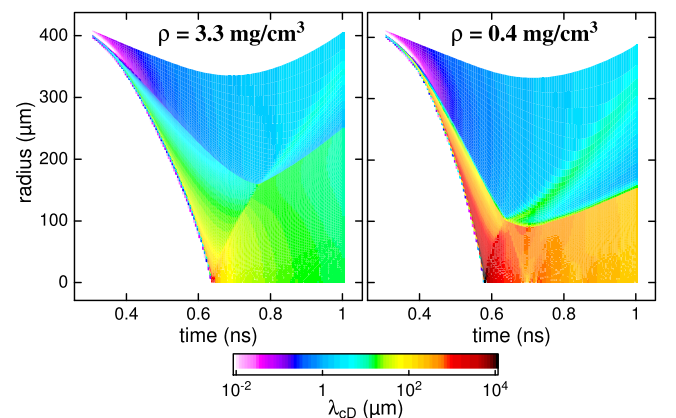

FIG. 4. Space-time plot of the collisional mean-free path of a thermal D ion λ_{cD} in the hydrodynamical simulation of the implosion in the high-density (left) and low-density (right) cases. The region of unshocked gas appearing in white to the left of the diagrams has $\lambda_{cD} < 0.01\ \mu m$.

is the collision frequency (in s^{-1}) between a thermal D ion and the electron population. In the above expressions for the frequencies, the ion density n_i and electron density n_e are in cm^{-3}, the ion temperature T_i and electron temperature T_e are in keV, and the Log Λ_{ab}'s are the Coulomb logarithms as defined, e.g., in Ref. 20. In the present case, a relevant dimension is the radius R of the imploded fuel around stagnation time. Inside the fuel near the fuel/pusher interface, λ_c/R is seen to reach maximum values of order ~ 0.07 in the high density case and ~ 10 in the low-density case.

A more relevant quantity to determine if diffusion effects should be expected over the duration of the implosion is the collisional diffusion coefficient $D = \lambda_c v_{th}$, which can be directly compared with the reference value $D_{ref} = R^2/T$, where R and T are typical values of distance and time in the experiment. In the present case, with $R \sim 100 \, \mu$m and $T \sim 200$ ps, the reference value is $D_{ref} \sim 5 \times 10^5$ cm^2/s. The diffusion coefficient for a thermal D ion is displayed in Fig. 5, where its value is seen to span several decades. It does become comparable with D_{ref} in the pusher near the fuel/pusher interface around stagnation and even larger in the low-density case. Diffusion of fuel ions into the pusher should thus be expected in these experiments, particularly in the low-density case.

III. KINETIC SIMULATION STRATEGY

As in the previous studies of the same kind,[14,17,21] hydrodynamical simulations of the targets as described in Section II are taken as a starting point, and the behaviour of the fuel (inside the fuel/pusher interface) is computed again using the kinetic model, taking the motion of the pusher in the course of time (assumed to be unchanged from the hydrodynamical simulation). The necessary boundary conditions for the kinetic calculation, namely, the distribution function of particles receding from the boundary into the fuel, imposed on the boundary, are constructed from the hydrodynamical quantities (density, velocity, and ion and electron temperatures) found there in the hydrodynamical calculation. As a result, the possible inter-diffusion of fuel and pusher material through the boundary is not treated in

the present work, the consequences of which will be discussed in Sec. V.

A. Kinetic calculations with FPION

The kinetic model used is the ion VFP code FPION, which has been described elsewhere.[13,14] Here, we will only briefly recall its main features.

The VFP equation for the velocity distribution function f_i of ions of species i with mass m_i and charge state Z_i, taking spherical symmetry into account, reads in spherical geometry (radius r, radial velocity v_r, and tangential velocity $v_\perp$), to lowest order in powers of the electron to ion mass ratio m_e/m_i

$$\frac{\partial f_i}{\partial t} + v_r \frac{\partial f_i}{\partial r} + \frac{v_\perp^2}{r} \frac{\partial f_i}{\partial v_r} - \frac{v_\perp v_r}{r} \frac{\partial f_i}{\partial v_\perp} + \frac{Z_i e \mathcal{E}}{m_i} \frac{\partial f_i}{\partial v_r}$$
$$= \sum_{j=1}^{n} \left(\frac{\partial f_i}{\partial t}\right)_{ij} + \left(\frac{\partial f_i}{\partial t}\right)_{ie}, \qquad (8)$$

where e is the elementary electric charge. The first term on the r.h.s. of the above equation accounts for Coulomb collisions between ion species i and the n ion species present, indexed by $j = 1$ to n

$$\left(\frac{\partial f_i}{\partial t}\right)_{ij} = \frac{16\pi^2 Z_i^2 Z_j^2 e^4}{m_i^2} \text{Log}\, \Lambda_{ij}$$
$$\times \frac{\partial}{\partial v_\alpha} \left[\frac{m_i}{m_j} \frac{\partial \mathcal{S}_j}{\partial v_\alpha} f_i - \frac{\partial^2 \mathcal{T}_j}{\partial v_\alpha \partial v_\beta} \frac{\partial f_i}{\partial v_\beta}\right],$$

where $\mathcal{S}_j$ and $\mathcal{T}_j$ are the so-called Rosenbluth potentials[22]

$$\mathcal{S}_j = -\frac{1}{4\pi} \int \frac{f_j(\vec{v'})}{|\vec{v} - \vec{v'}|} d^3 v'$$

and

$$\mathcal{T}_j = -\frac{1}{8\pi} \int |\vec{v} - \vec{v'}| f_j(\vec{v'}) d^3 v'.$$

The last term in the r.h.s. of Eq. (8) accounts for electron-ion collisions

$$\left(\frac{\partial f_i}{\partial t}\right)_{ie} = \frac{1}{2\tau_{ei}} \frac{\partial}{\partial v_\alpha} \left[(v_\alpha - u_{i\alpha})f_i(\vec{v}) + \frac{k_B T_e}{m_i} \frac{\partial f_i}{\partial v_\alpha}(\vec{v})\right],$$

where τ_{ei} is the electron-ion collisional energy exchange time

$$\tau_{ei} = \frac{3 m_i (k_B T_e)^{3/2}}{8(2\pi m_e)^{1/2} Z_i^2 e^4 n_e \, \text{Log}\, \Lambda_{ie}}.$$

In all of the above, n_s, $\vec{u}_s$, and T_s are the density, velocity, and temperature of species s (including ions and electrons); Log Λ_{ab} is the Coulomb logarithm for collisions between particles of species a and b; and $\mathcal{E}$ is the electric field, which in the limit of a vanishing electron mass (or a vanishing plasma period) reads
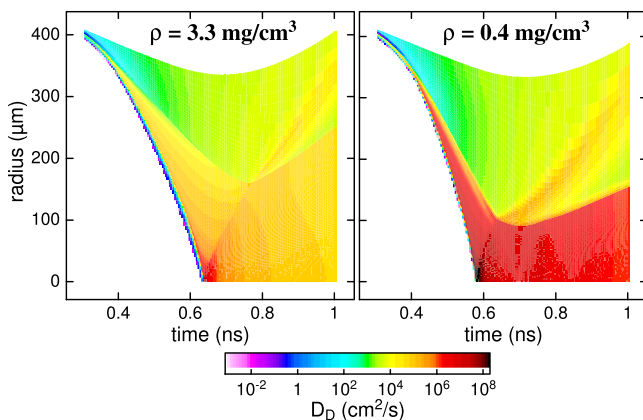

FIG. 5. Space-time plot of the collisional diffusion coefficient of a thermal D ion D_D in the hydrodynamical simulation of the implosion in the high-density (left) and low-density (right) cases. The region of unshocked gas appearing in white to the left of the diagrams has $D_D < 0.001$ cm^2/s.

$$\mathcal{E} = -\frac{1}{en_e}\frac{\partial P_e}{\partial r},$$

where P_e is electron pressure. Finally, the electron temperature T_e is governed by the conservation equation for the electron energy density W_e

$$\frac{\partial W_e}{\partial t} + \frac{1}{r^2}\frac{\partial}{\partial r}\left(r^2 u_e W_e\right) + \frac{1}{r^2}\frac{\partial}{\partial r}\left(r^2 u_e\right)P_e - \frac{1}{r^2}\frac{\partial}{\partial r}\left(r^2 \kappa_e \frac{\partial T_e}{\partial r}\right)$$
$$= \sum_{j=1}^{n}\frac{3n_j}{2\tau_{ej}}(T_j - T_e) + \left(\frac{\partial W_e}{\partial t}\right)_{rad},$$

where κ_e is the (possibly flux-limited[23,24]) Spitzer-Härm[25] thermal conductivity and the last term on the r.h.s. accounts for Bremsstrahlung losses. The energy density W_e and pressure P_e are found from the electron fluid equation of state, taking quantum degeneracy into account.

The D^3He gas is treated as a mix of two different ion species, each with its own velocity distribution function, discretized on a grid consisting of 200 cells in radius × 128 cells in radial velocity × 64 cells in perpendicular velocity. The initial conditions of the calculations are constructed from the profiles of the fluid quantities in the hydrodynamical simulations of the targets presented in Sec. II B at time $t = 350$ ps. The boundary condition at the fuel-pusher interface is extracted from the hydrodynamical simulation results, with some adaptation to try to properly take into account the large T_i gradients across the interface (see Fig. 2). Namely, the ion temperature for D and ^3He is taken from slightly inside the pusher to take into account the (probably unphysical) large T_i jump across the interface found in the hydrodynamical simulation. In the calculations presented below, a flux limiter value of 0.07 was applied to thermal electron conduction. The rate of nuclear reactions and reactivity-weighted ion temperatures are computed in a post-processing step. Diagnostics are derived, as described in Section III B.

B. Nuclear diagnostics from FPION

The rate of a nuclear reaction involving one ion of species i with another one of species j (number of reactions per unit volume and unit time) is defined as

$$R_{ij} = \frac{1}{1 + \delta_{ij}}\int f_i(\vec{v_i})f_j(\vec{v_j})|\vec{v_i} - \vec{v_j}|\sigma_{ij}(|\vec{v_i} - \vec{v_j}|)d^3 v_i d^3 v_j,$$

where the reaction cross-section $\sigma_{ij}(|\vec{v_i} - \vec{v_j}|)$ is taken from Ref. 26. From the reaction rate, various quantities can be derived as diagnostics of an implosion, as described in Sec. II. The quantities defined in Eqs. (4)–(7) are calculated straightforwardly by FPION from the latter expressions in a post-processing step after the simulations are run.

The reaction-weighted fuel ion temperature is computed in the following way. The classical theory from Brysk[27] is used to analyze fusion product spectra from a given reaction $1 + 2 \rightarrow 3 + 4$, according to Ref. 16. Here, we revisit this theory, keeping possibly different temperatures for species 1 and 2. Equation (35) from Ref. 27 becomes

$$\langle(E_3 - \langle E_3\rangle)^2\rangle = \frac{2m_3 m_4}{m_3 + m_4}Q\frac{\langle V^2\rangle}{3}$$
$$= \frac{2m_3 m_4}{(m_3 + m_4)^2}Q\frac{m_1 k_B T_1 + m_2 k_B T_2}{m_1 + m_2},$$

where E_3 is the energy of a collected particle of species 3, Q is the energy released in one reaction, $\langle V^2\rangle$ is the mean square of the center-of-mass velocity, and the angular brackets stand for averaging over the distribution functions of the reacting particles

$$\langle.\rangle = \frac{1}{n_1 n_2}\int .f_1(\vec{v_1})f_1(\vec{v_2})d^3 v_1 d^3 v_2.$$

Note that this averaging process does not take into account any weighting from reaction $\langle\sigma v\rangle$. See Ref. 28 for a lead toward a more consistent treatment. The width of the collected particle spectrum is seen to be proportional to an average of the temperatures of the reacting ions, weighted by the respective particle masses. Thus, here the following *ad hoc* reactivity weighting is used to get to the final burn-averaged fuel temperature

$$T_{ij} = \frac{1}{Y_{ij}}\int\frac{m_i T_i(r,t) + m_j T_j(r,t)}{m_i + m_j}R_{ij}(r,t)4\pi r^2 dr dt, \quad (9)$$

where Y_{ij} is the total yield defined in Eq. (6).

IV. KINETIC SIMULATION RESULTS

A. Distribution functions at shock convergence

The parallel distribution functions

$$f_{i\parallel}(r, v_r) = \int_0^\infty f_i(r, v_r, v_\perp)2\pi v_\perp dv_\perp$$

are calculated from the simulation results for D and ^3He and plotted in Figs. 6 and 7 at the time when the main shock convergence is reached in the corresponding hydrodynamical simulations. Instead of a well-defined localized shock front, what is found in the kinetic simulations is an extended region where the upstream and downstream ion populations coexist without relaxing, leading to a two-component structure in the
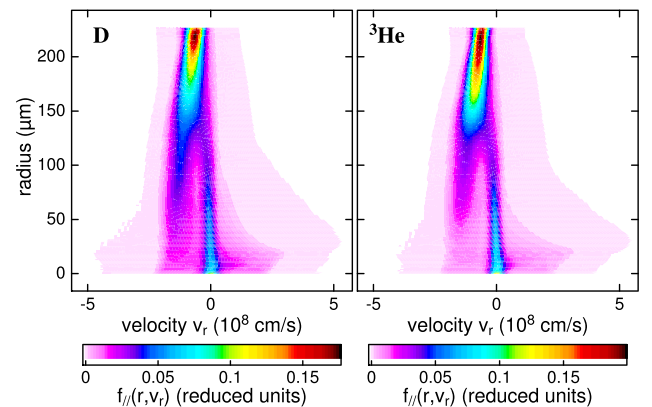

FIG. 6. Parallel distribution functions for both ion species in the high-density case at shock convergence ($t = 600$ ps).
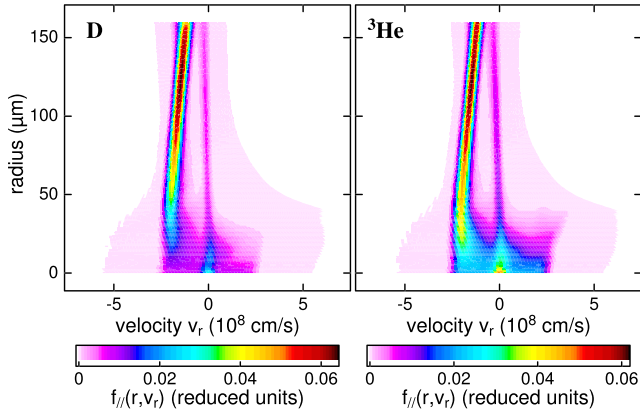
FIG. 7. Parallel distribution functions for both ion species in the low-density case at shock convergence ($t = 580$ ps).

resulting velocity distribution, particularly in the low-density (less collisional) case. Such distribution features, very far from thermodynamic equilibrium, cannot be taken into account in transport models based on perturbative arguments such as the RIK model.[12] The interpenetrating-plasma structure found in our simulations is quite similar to what has been seen in various studies involving plasma collisions.[13,29–37]

B. Kinetic results in the course of time

In addition to deviations from thermodynamic equilibrium for each species, there are also deviations of the hydrodynamical quantities of each ion species with respect to the other. Figs. 8 and 9 display space-time plots of the relative differences in density and ion temperature between ^{3}He and D which develop as the implosion proceeds, in the high- and low-density cases, respectively. These plots can be directly compared with Figs. 1 and 2 of Ref. 17 in the case of shock-ignition DT capsules. A sizeable amount of species separation and ion temperature decoupling is observed in the kinetic calculations as well as in the experimental data.[11] These effects have consequences on reactivities and fusion-averaged ion temperatures, in addition to the direct consequences from the distorted distribution functions as seen in Figs. 6 and 7. In particular, temperature decoupling provides
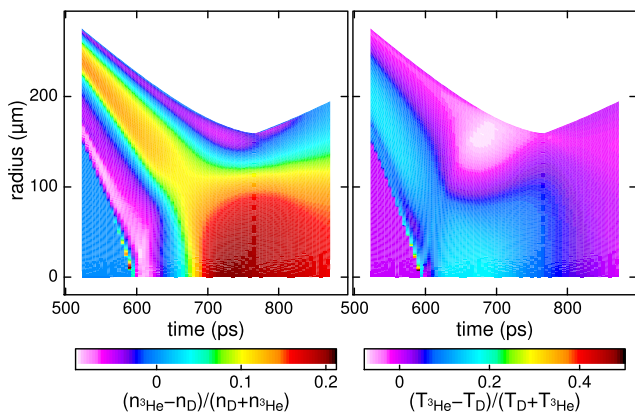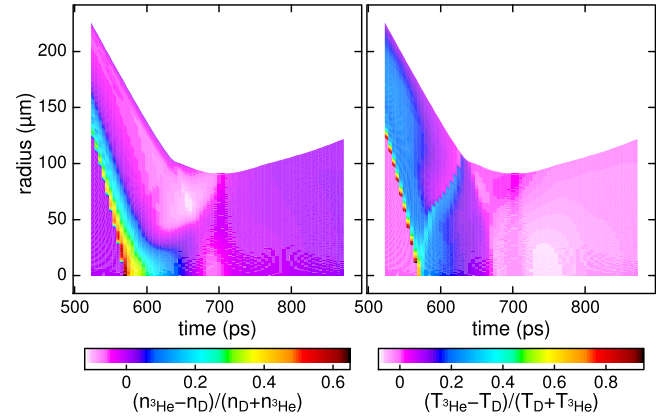
a natural explanation for the fact that T_{D^3He} is systematically found higher than T_{DD} in experiments (see Tables I and II in view of Eq. (9), noticing the specific weighting of ion temperatures in the latter expression), much in the same way as discussed in Ref. 17. The maximum temperature ratio between ^{3}He and D in Fig. 8 is $T_{^3He}/T_D \sim 1.35$, which is almost exactly the maximum value predicted for the shocked plasma ($= 4/3$) in Ref. 11.

The nuclear reactivities as functions of space and time for reactions (2) and (3) and the corresponding burn-averaged ion temperatures are displayed in Figs. 10 and 11 for the high- and low-density cases, respectively. In the low-density case, most of the reactions occur during the second fusion burst (around 680 ps) caused by the shock reflected from the pusher back into the fuel, in a region extending all the way to the pusher interface. The outer fuel layers with larger values of the radius r contribute more to the total yield due to the strong increase in the volume element $4\pi r^2 dr$, although the local reactivity is lower than during the first combustion burst which takes place in the target center around 620 ps.

The time-integrated emissivities, as defined in Eq. (4), are computed from the reactivity values as functions of

FIG. 9. Relative differences between ^{3}He and D as regards density ($(n_{^3He} - n_D)/(n_D + n_{^3He})$) (left) and ion temperature ($(T_{^3He} - T_D)/(T_D + T_{^3He})$) (right) as functions of space and time in the low-density case.

FIG. 8. Relative differences between ^{3}He and D as regards density $(n_{^3He} - n_D)/(n_D + n_{^3He})$ (left) and ion temperature $(T_{^3He} - T_D)/(T_D + T_{^3He})$ (right) as functions of space and time in the high-density case.

FIG. 10. Nuclear reactivities as a function of space and time in the high-density case. The total yields and burn-averaged temperatures are mentioned on the respective panels.
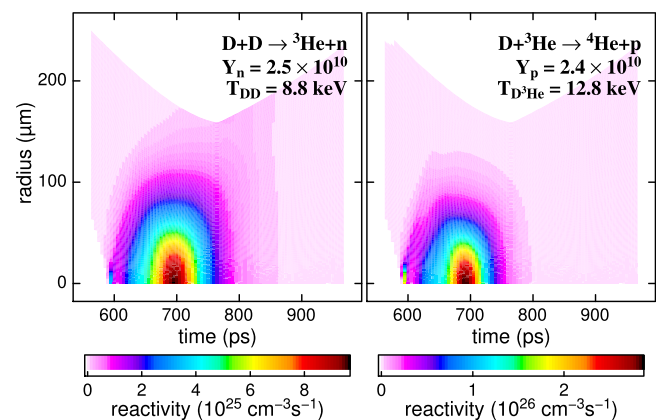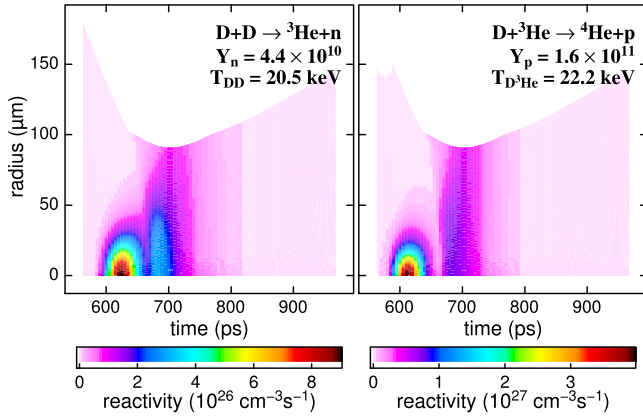
FIG. 11. Nuclear reactivities as a function of space and time in the low-density case. The total yields and burn-averaged temperatures are mentioned on the respective panels.

radius and time, as displayed in Figs. 10 and 11. The results for reactions (1) and (3) in both the high- and low-density cases are gathered in Fig. 12, for easier comparison with experimental data and their hydrodynamical counterparts in Figs. 5 and 8 of Ref. 9, respectively. In the high-density case, the FPION profiles are seen to agree qualitatively and also quantitatively with the experimental ones, taking into account the uncertainty in the reconstruction procedure from raw penumbral image data, whereas the hydrodynamical DUED simulations are too high by a factor of about 5 to 10, leading to an integrated yield over-estimated by a factor 2 to 3. However, in the low-density case, the FPION profiles, although closer to the experimental ones than the best DUED results, are still an order of magnitude too large. They are also qualitatively unsatisfactory: an unphysical reactivity bump due to reactions occurring near the fuel/pusher interface is found in the kinetic simulation (around $r \sim 90\,\mu m$ in Fig. 12). In that respect, the kinetic simulation is not better than the fluid one in the low-density case. The presence of this erroneous feature in the vicinity of the interface in
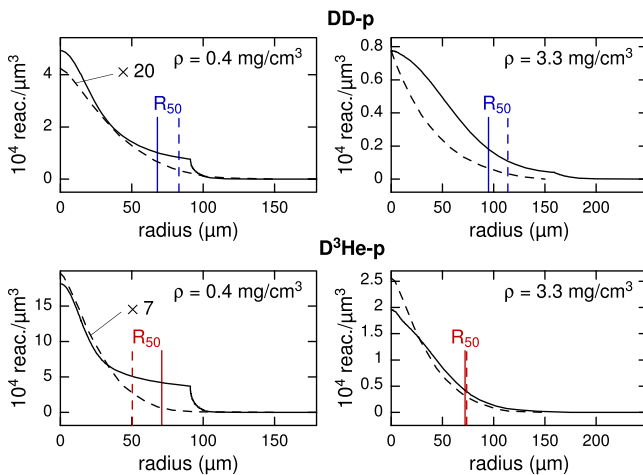
models (either kinetic or fluid) which do not take into account ion diffusion through the interface clearly suggest that the latter effect is important.

The surface brightness, as defined in Eq. (5), is computed from the reactivity as a function of radius and time. The results for reactions (1) and (3) in both the high- and low-density cases are gathered in Fig. 13, for easier comparison with the experimental data and their hydrodynamical counterparts in Fig. 7 of Ref. 9. In the high-density case, the FPION profiles are seen to reach a reasonable agreement (for DD protons) or even very good agreement (for D^{3}He protons) with the experimental ones, whereas the results of hydrodynamical modeling with the LASNEX code are too high by a factor of 2 to 5, depending on the reaction considered and whether ion diffusion is taken into account or not. However, in the low-density case, the FPION profiles are once again an order of magnitude above the experimental ones, although they do find the correct qualitative shape, with the maximum brightness value at target center rather than near the pusher interface. On the other hand, the profiles from hydrodynamical modeling either display an unsatisfactory shape (without kinetic corrections) or get too low brightness values (when ion diffusion is taken into account). The better qualitative agreement of the kinetic calculation can be attributed to the correct treatment of highly distorted velocity distribution in the target interior, although the modeling of the interaction with the pusher needs to be improved.

C. Comparison with hydrodynamical results at peak reactivity

To better understand why the hydrodynamical and kinetic simulations deviate from each other and from the experimental data (apart from the kinetic simulation in the high-density case which agrees quite well with experiment), we focussed on the state of the plasma when the overall reaction rate (in reactions per second from the whole fuel) is the highest, which occurs at time $t \approx 690$ ps in both the

FIG. 12. Fusion emissivities as a function of radius for the DD-p (top) and D^{3}He-p (bottom) reactions, in the high-density (right) and low-density (left) cases. The median radius R_{50} is indicated in each case. This figure can be directly compared with Figs. 8 and 5 of Ref. 9. For easier comparison, the experimental curves from the latter figure are reproduced here as dashed lines (notice the factors applied to these curves in the low-density case).

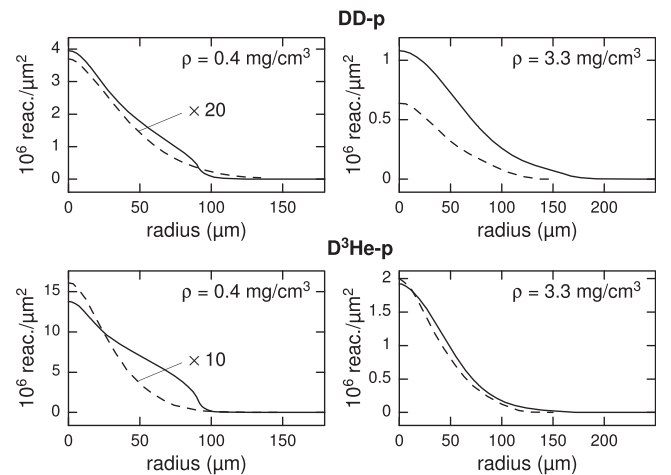FIG. 13. Fusion surface brightness as a function of radius for the DD-p (top) and D^{3}He-p (bottom) reactions, in the high-density (right) and low-density (left) cases. This figure can be directly compared with Fig. 7 of Ref. 9. For easier comparison, the experimental curves from the latter figure are reproduced here as dashed lines (notice the factors applied to these curves in the low-density case).
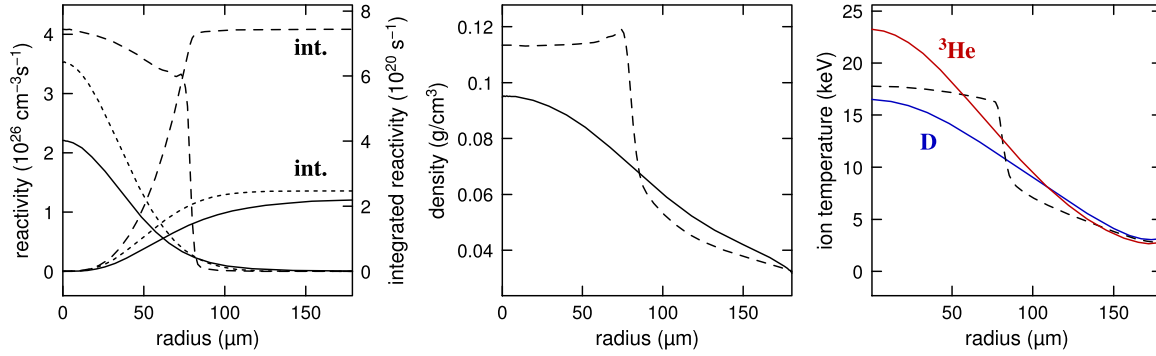
FIG. 14. Spatial profiles of reactivity-related quantities in the fuel at the time of maximum proton production rate ($t = 690$ ps) for the D^{3}He reaction in the high-density case. Dashed lines refer to the hydrodynamical simulation results, solid and dotted lines refer to kinetic results. Left: profiles of the local reaction rate and the volume-integrated rate (curves labelled "int."). Solid lines stand for the exact kinetic rates, dotted lines for the rates obtained from the kinetic calculation but using average-Maxwellian distributions. Middle and right: profiles of the density and ion temperature at the same time. In the kinetic case, separate temperature profiles are given for D and ^{3}He.

high- and low-density cases. Figures 14 and 15 display profiles of reactivity-related quantities in the fuel at that time, for the high- and low-density cases, respectively. These include the local reaction rate $R_{ij}(R, t = 690\text{ps})$ for reaction (3) and its partial volume-integrated rate

$$\int_0^R R_{ij}(r, t = 690\text{ps})4\pi r^2 dr$$

as functions of R, together with the density and ion temperature profiles, which have a direct influence on reactivity.

In the higher-density case, the kinetic simulation is in better agreement with experimental data than hydrodynamical calculations, even though the plasma is more collisional than in the lower-density case, from which the hydrodynamical model might have been expected to perform better. From the plots in Fig. 14, the excess rate in the hydro calculation is seen to arise mainly from the downstream layer of the rather sharp reflected shock around $R \approx 75\,\mu m$, where both the density and the ion temperature are appreciably higher than their kinetic counterparts. But from Fig. 4, we find that the collisional mean-free-path for ions in that space-time region is several tens of microns, which clearly precludes such a well-defined shock front to occur. Obviously, since plasma

shock-front transition layers are known[38] to span at least several tens of mean-free-paths, the hydro profiles are grossly in error in that region. A better agreement of hydro codes with experiment (and kinetic calculations) is expected to be reached by using a more physical description of shock fronts, at least involving physical viscosity[39] (possibly with specifically tuned multipliers) or some revised pseudo-viscosity so as not to obtain sharp shock fronts when physics tells us that they should not show up.

In the lower-density case, the simulated yields are well above the experimentally measured value, for the kinetic model and even more so for the hydrodynamical model. The excess reactivity of the latter over the former is seen in Fig. 15 to result mainly from a strongly over-estimated ion temperature. On the other hand, the density calculated by the kinetic model is a factor ≈ 2 above the hydrodynamical value, so that the total fuel mass in the capsule is found too large by about the same factor. This clearly points at a bad modeling of the boundary condition on the fuel/pusher interface in the kinetic model. By the way, if we assume the density to be half what is found in the calculation to compensate for this error, then the yield will decrease to a quarter of the value found, which would bring it much closer to the experimental data (see Table II). For the ion temperature, from the good
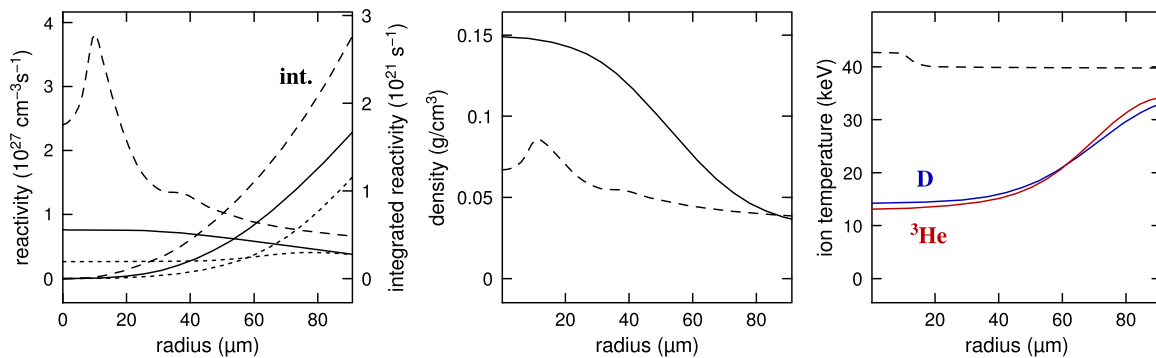
FIG. 15. Spatial profiles of reactivity-related quantities in the fuel at the time of maximum proton production rate ($t = 690$ ps) for the D^{3}He reaction in the low-density case. Dashed lines refer to the hydrodynamical simulation results, solid and dotted lines refer to kinetic results. Left: profiles of the local reaction rate and the volume-integrated rate (curves labelled "int."). Solid lines stand for the exact kinetic rates, dotted lines for the rates obtained from the kinetic calculation but using average-Maxwellian distributions. Middle and right: profiles of the density and ion temperature at the same time. In the kinetic case, separate temperature profiles are given for D and ^{3}He.

agreement of its reaction-averaged value with the experimental data, we can assume it to be satisfactorily rendered by the kinetic calculation.

Other discrepancies between the hydro and kinetic calculations seem to play a more limited role as far as the yield is concerned in both cases. The non-Maxwellian character of the ion distribution functions, which is evidenced by the difference between the exact and Maxwellian-averaged rates in Figs. 14 and 15, occurs in the central part of the fuel, but is not significant in the region where most of the yield is produced, namely, in the shock front region in the high-density case and in the outer third of the fuel radius in the low-density case. The same is true for the temperature decoupling between D and ^{3}He, which, in addition, is quite negligible at the time of peak reactivity in the low-density case.

V. DISCUSSION

In the high-density case, the kinetic FPION simulation satisfactorily renders the experimental results, without having to resort to additional *ad hoc* elements. The agreement is much better than with plain hydrodynamical simulations. When the latter include additional heuristic modeling of ion-kinetic effects through the RIK package, the observables which are not used to constrain the parameter tuning inherent in this model (e.g., the median burn radius R_{50}) are still not rendered as satisfactorily as by the kinetic model. In contrast, in the low-density case, large discrepancies remain, probably due to significant phenomena occurring near the pusher. This would be consistent with the strongly out-of-equilibrium distributions (displaying a two-component structure instead of a perturbed Maxwellian, see Fig. 7) found in the gas all the way to the gas/pusher interface in this case, whereas in the higher-density case the distribution is less distorted and remains single-peaked in the vicinity of the shell (see Fig. 6).

The surface brightness diagnostic tends to emphasize processes occurring in the outer layers of the gas (a "limb-brightening" effect leading to profiles peaking away from the centre, cf. Fig. 7 of Ref. 9) and is thus more sensitive than reactivity itself to flaws in the modeling of diffusion through the interface.

The problem here is twofold. On one hand, the double-peaked structure displayed by the ion velocity distribution close to the shell in the low-density case might be amplified (if not entirely caused) by the conflicting constraints imposed on ingoing and outgoing particles by the boundary condition. On the other hand, due to the lower collisionality in the low-density case, a deficient description of the phenomena occurring near the fuel/pusher interface might influence the whole fuel, which might be the reason why the yield is grossly overestimated. An improved modeling is needed for the ingoing part of the distribution, which is used as a boundary condition for the FPION simulation in the present situation. Let us notice that the boundary modeling used in the present work does not preserve the total amount of gas inside the shell. While ingoing particles are taken from a Maxwellian distribution defined from the density, fluid velocity, and temperature found in the hydrodynamical simulation, the outgoing part of the distribution is just a result of the kinetic calculation and cannot be modified. As a result, the mass and energy currents through the fuel/pusher interface do not necessarily vanish. Accordingly, the collisional mean-free path for a deuterium ion entering the SiO_2 plasma of the pusher is expected to remain quite large in the low-density case (as can be estimated from the hydrodynamical results, see Fig. 4). But these currents cannot be expected to satisfactorily render the diffusion of inside gas through the interface. What is needed is a genuinely self-consistent kinetic treatment of this diffusion.

The question of the fuel/pusher inter-diffusion has been actually investigated, including from the experimental point of view, see Refs. 10 and 40. The experiments described in Ref. 10, dealing with the implosion of ^{3}He gas by a CD (deuterated plastic) shell, have quite convincingly evidenced a significant amount of atomic mixing between the ion species from the inner gas and from the pusher. As a matter of fact, their interpretation[40] by codes[12] with a heuristic modeling of ion diffusion through the gas/pusher interface does qualitatively render the results of these experiments.

VI. SUMMARY AND PERSPECTIVES

As a conclusion, VFP kinetic simulations of D^{3}He gas ICF target implosions are in good agreement with experimental results in the case of a relatively higher-density, more collisional material. The various available experimental data are much better rendered from first principles than by the hydrodynamical simulations. When the latter are supplemented with a heuristic modeling of the ion-kinetic effects involved, there is still better agreement of the kinetic model on these observables which are not used as constraints during the tuning phase of the heuristic package. This is an indication that the important physical mechanisms at play in these targets have been identified, namely, the strongly kinetic behaviour of the ions of the central part of the gas, leading in the early stage of the implosion to two-beam-like distribution functions which are quite far from perturbed Maxwellians.

In the case of lower-density gas, there is evidence that the poor agreement obtained with experimental results is (at least partly) due to an improper treatment of the interaction between the inside gas and the pusher. We now intend to improve our ion-kinetic model to be able to handle the interaction of the light ions of the inside gas with the heavier, much more collisional ions of the pusher, leading to a self-consistent treatment of the fuel/pusher system. In addition, the effect of varying the deuterium abundance ratio from the equimolar value of 0.5 used in this work, which is particularly important in the low-density case,[11] could then be appropriately investigated in the frame of our kinetic model.

[1]J. D. Lindl, O. L. Landen, M. J. Edwards, E. I. Moses, and the NIC Team, Phys. Plasmas **21**, 020501 (2014).
[2]J. J. Duderstadt and G. A. Moses, *Inertial Confinement Fusion* (John Wiley and Sons, New York, 1982).

[3]J. D. Lindl, P. A. Amendt, R. L. Berger, S. G. Glendinning, S. H. Glenzer, S. W. Haan, R. L. Kauffman, O. L. Landen, and L. J. Suter, Phys. Plasmas **11**, 339 (2004).

[4]S. Atzeni and J. Meyer-ter-Vehn, *The Physics of Inertial Fusion* (Clarendon Press, Oxford, 2004).

[5]W. J. Krauser, N. M. Hoffman, D. C. Wilson, B. H. Wilde, W. S. Varnum, D. B. Harris, F. J. Swenson, P. A. Bradley, S. W. Haan, S. M. Pollaine, A. S. Wan, J. C. Moreno, and P. A. Amendt, Phys. Plasmas **3**, 2084 (1996).

[6]S. W. Haan, J. D. Lindl, D. A. Callahan, D. S. Clark, J. D. Salmonson, B. A. Hammel, L. J. Atherton, R. C. Cook, M. J. Edwards, S. Glenzer, A. V. Hamza, S. P. Hatchett, M. C. Herrmann, D. E. Hinkel, D. D. Ho, H. Huang, O. S. Jones, J. Kline, G. Kyrala, O. L. Landen, B. J. MacGowan, M. M. Marinak, D. D. Meyerhofer, J. L. Milovich, K. A. Moreno, E. I. Moses, D. H. Munro, A. Nikroo, R. E. Olson, K. Peterson, S. M. Pollaine, J. E. Ralph, H. F. Robey, B. K. Spears, P. T. Springer, L. J. Suter, C. A. Thomas, R. P. Town, R. Vesey, S. V. Weber, H. L. Wilkens, and D. C. Wilson, Phys. Plasmas **18**, 051001 (2011).

[7]M. J. Rosenberg, A. B. Zylstra, F. H. Séguin, H. G. Rinderknecht, J. A. Frenje, M. Gatu Johnson, H. Sio, C. J. Waugh, N. Sinenian, C. K. Li, R. D. Petrasso, P. W. McKenty, M. Hohenberger, P. B. Radha, J. A. Delettrez, V. Yu. Glebov, R. Betti, V. N. Goncharov, J. P. Knauer, T. C. Sangster, S. LePape, A. J. Mackinnon, J. Pino, J. M. McNaney, J. R. Rygg, P. A. Amendt, C. Bellei, L. R. Benedetti, L. Berzak Hopkins, R. M. Bionta, D. T. Casey, L. Divol, M. J. Edwards, S. Glenn, S. H. Glenzer, D. G. Hicks, J. R. Kimbrough, O. L. Landen, J. D. Lindl, T. Ma, A. MacPhee, N. B. Meezan, J. D. Moody, M. J. Moran, H.-S. Park, B. A. Remington, H. Robey, M. D. Rosen, S. C. Wilks, R. A. Zacharias, H. W. Herrmann, N. M. Hoffman, G. A. Kyrala, R. J. Leeper, R. E. Olson, J. D. Kilkenny, and A. Nikroo, Phys. Plasmas **21**, 122712 (2014).

[8]M. J. Rosenberg, H. G. Rinderknecht, N. M. Hoffman, P. A. Amendt, S. Atzeni, A. B. Zylstra, C. K. Li, F. H. Séguin, H. Sio, M. Gatu Johnson, J. A. Frenje, R. D. Petrasso, V. Yu. Glebov, C. Stoeckl, W. Seka, F. J. Marshall, J. A. Delettrez, T. C. Sangster, R. Betti, V. N. Goncharov, D. D. Meyerhofer, S. Skupsky, C. Bellei, J. Pino, S. C. Wilks, G. Kagan, K. Molvig, and A. Nikroo, Phys. Rev. Lett. **112**, 185001 (2014).

[9]M. J. Rosenberg, F. H. Séguin, P. A. Amendt, S. Atzeni, H. G. Rinderknecht, N. M. Hoffman, A. B. Zylstra, C. K. Li, H. Sio, M. Gatu Johnson, J. A. Frenje, R. D. Petrasso, V. Yu. Glebov, C. Stoeckl, W. Seka, F. J. Marshall, J. A. Delettrez, T. C. Sangster, R. Betti, S. C. Wilks, J. Pino, G. Kagan, K. Molvig, and A. Nikroo, Phys. Plasmas **22**, 062702 (2015).

[10]H. G. Rinderknecht, H. Sio, C. K. Li, A. B. Zylstra, M. J. Rosenberg, P. Amendt, J. Delettrez, C. Bellei, J. A. Frenje, M. Gatu Johnson, F. H. Séguin, R. D. Petrasso, R. Betti, V. Yu. Glebov, D. D. Meyerhofer, T. C. Sangster, C. Stoeckl, O. Landen, V. A. Smalyuk, S. Wilks, A. Greenwood, and A. Nikroo, Phys. Rev. Lett. **112**, 135001 (2014).

[11]H. G. Rinderknecht, M. J. Rosenberg, C. K. Li, N. M. Hoffman, G. Kagan, A. B. Zylstra, H. Sio, J. A. Frenje, M. Gatu Johnson, F. H. Séguin, R. D. Petrasso, P. Amendt, C. Bellei, S. Wilks, J. Delettrez, V. Yu. Glebov, C. Stoeckl, T. C. Sangster, D. D. Meyerhofer, and A. Nikroo, Phys. Rev. Lett. **114**, 025001 (2015).

[12]N. M. Hoffman, G. B. Zimmerman, K. Molvig, H. G. Rinderknecht, M. J. Rosenberg, B. J. Albright, A. N. Simakov, H. Sio, A. B. Zylstra, M. Gatu Johnson, F. H. Séguin, J. A. Frenje, C. K. Li, R. D. Petrasso, D. M. Higdon, G. Srinivasan, V. Yu. Glebov, C. Stoeckl, W. Seka, and T. C. Sangster, Phys. Plasmas **22**, 052707 (2015).

[13]O. Larroche, Phys. Fluids B **5**, 2816 (1993).

[14]O. Larroche, Eur. Phys. J. D **27**, 131 (2003).

[15]F. H. Séguin, J. L. DeCiantis, J. A. Frenje, S. Kurebayashi, C. K. Li, J. R. Rygg, C. Chen, V. Berube, B. E. Schwartz, R. D. Petrasso, V. A. Smalyuk, F. J. Marshall, J. P. Knauer, J. A. Delettrez, P. W. McKenty, D. D. Meyerhofer, S. Roberts, T. C. Sangster, K. Mikaelian, and H. S. Park, Rev. Sci. Instrum. **75**, 3520 (2004).

[16]J. A. Frenje, R. Bionta, E. J. Bond, J. A. Caggiano, D. T. Casey, C. Cerjan, J. Edwards, M. Eckart, D. N. Fittinghoff, S. Friedrich, V. Yu. Glebov, S. Glenzer, G. Grim, S. Haan, R. Hatarik, S. Hatchett, M. Gatu Johnson, O. S. Jones, J. D. Kilkenny, J. P. Knauer, O. Landen, R. Leeper, S. Le Pape, R. Lerche, C. K. Li, A. Mackinnon, J. McNaney, F. E. Merrill, M. Moran, D. H. Munro, T. J. Murphy, R. D. Petrasso, R. Rygg, T. C. Sangster, F. H. Sguin, S. Sepke, B. Spears, P. Springer, C. Stoeckl, and D. C. Wilson, Nucl. Fusion **53**, 043014 (2013).

[17]A. Inglebert, B. Canaud, and O. Larroche, Europhys. Lett. **107**, 65003 (2014).

[18]S. Atzeni, Comput. Phys. Commun. **43**, 107 (1986).

[19]S. Atzeni, A. Schiavi, F. Califano, F. Cattani, F. Cornolti, D. Del Sarto, T. V. Liseykina, A. Macchi, and F. Pegoraro, Comput. Phys. Commun. **169**, 153 (2005).

[20]S. I. Braginskii, "Transport processes in a plasma," in *Reviews of Plasma Physics*, Vol. 1, edited by M. A. Leontovich (Consultants Bureau, New York, 1965), p. 205.

[21]O. Larroche, Phys. Plasmas **19**, 122706 (2012).

[22]M. N. Rosenbluth, W. M. MacDonald, and D. L. Judd, Phys. Rev. **107**, 1 (1957).

[23]D. Colombant and W. Manheimer, J. Comput. Phys. **229**, 4369 (2010).

[24]F. Vidal, J.-P. Matte, M. Casanova, and O. Larroche, Phys. Plasmas **2**, 1412 (1995).

[25]L. Spitzer and R. Härm, Phys. Rev. **89**, 977 (1953).

[26]H.-S. Bosch and G. M. Hale, Nucl. Fusion **32**, 611 (1992).

[27]H. Brysk, Plasma Phys. **15**, 611 (1973).

[28]B. Appelbe and J. Chittenden, Plasma Phys. Controlled Fusion **53**, 045002 (2011).

[29]P. Glas, M. Schnürer, E. Förster, and I. Uschmann, Opt. Commun. **86**, 271 (1991).

[30]R. A. Bosch, R. L. Berger, B. H. Failor, N. D. Delamater, G. Charatis, and R. L. Kauffman, Phys. Fluids B **4**, 979 (1992).

[31]P. W. Rambo and R. J. Procassini, Phys. Plasmas **2**, 3130 (1995).

[32]C. Chenais-Popovics, P. Renaudin, O. Rancu, F. Gilleron, J.-C. Gauthier, O. Larroche, O. Peyrusse, M. Dirksmöller, P. Sondhauss, T. Missalla, I. Uschmann, E. Förster, O. Renner, and E. Krouský, Phys. Plasmas **4**, 190 (1997).

[33]L. O. Silva, R. A. Fonseca, J. W. Tonge, J. M. Dawson, W. B. Mori, and M. V. Medvedev, Astrophys. J. **596**, L121 (2003).

[34]C. Courtois, R. A. D. Grundy, A. D. Ash, D. M. Chambers, N. C. Woolsey, R. O. Dendy, and K. G. McClements, Phys. Plasmas **11**, 3386 (2004).

[35]G. F. Swadling, S. V. Lebedev, A. J. Harvey-Thompson, W. Rozmus, G. C. Burdiak, L. Suttle, S. Patankar, R. A. Smith, M. Bennett, G. N. Hall, F. Suzuki-Vidal, S. Bland, and J. Yuan, Phys. Plasmas **22**, 072706 (2015).

[36]C. M. Huntington, F. Fiuza, J. S. Ross, A. B. Zylstra, R. P. Drake, D. H. Froula, G. Gregori, N. L. Kugland, C. C. Kuranz, M. C. Levy, C. K. Li, J. Meinecke, T. Morita, R. D. Petrasso, C. Plechaty, B. A. Remington, D. D. Ryutov, Y. Sakawa, A. Spitkovsky, H. Takabe, and H.-S. Park, Nat. Phys. **11**, 173 (2015).

[37]P. McQuillen, J. Castro, S. Bradshaw, and T. C. Killian, Phys. Plasmas **22**, 043514 (2015).

[38]M. Casanova, O. Larroche, and J.-P. Matte, Phys. Rev. Lett. **67**, 2143 (1991).

[39]T. Yabe and K. A. Tanaka, Laser Part. Beams **7**, 259 (1989).

[40]H. G. Rinderknecht, H. Sio, C. K. Li, N. Hoffman, A. B. Zylstra, M. J. Rosenberg, J. A. Frenje, M. Gatu Johnson, F. H. Séguin, R. D. Petrasso, R. Betti, V. Yu Glebov, D. D. Meyerhofer, T. C. Sangster, W. Seka, C. Stoeckl, G. Kagan, K. Molvig, C. Bellei, P. Amendt, O. Landen, J. R. Rygg, V. A. Smalyuk, S. Wilks, A. Greenwood, and A. Nikroo, Phys. Plasmas **21**, 056311 (2014).